Monthly Notices
of the
ROYAL ASTRONOMICAL SOCIETY

MNRAS **487,** 3007–3020 (2019)
Advance Access publication 2019 May 31

doi:10.1093/mnras/stz1486

Kinematics of $z \geq 6$ galaxies from [C II] line emission

M. Kohandel,[1★] A. Pallottini,[1,2] A. Ferrara,[1] A. Zanella,[3] C. Behrens,[4] S. Carniani,[1] S. Gallerani[1] and L. Vallini[5,6]

[1]*Scuola Normale Superiore, Piazza dei Cavalieri 7, I-56126 Pisa, Italy*
[2]*Centro Fermi, Museo Storico della Fisica e Centro Studi e Ricerche 'Enrico Fermi', Piazza del Viminale 1, I-00184 Roma, Italy*
[3]*European Southern Observatory, Karl Schwarzschild Straße 2, D-85748 Garching, Germany*
[4]*Institut für Astrophysik, Georg-August Universität Göttingen, Friedrich-Hundt-Platz 1, D-37077 Göttingen, Germany*
[5]*Leiden Observatory, Leiden University, PO Box 9500, NL-2300 RA Leiden, the Netherlands*
[6]*Nordita, KTH Royal Institute of Technology and Stockholm University Roslagstullsbacken 23, SE-106 91 Stockholm, Sweden*

Accepted 2019 May 24. Received 2019 May 20; in original form 2019 March 13

ABSTRACT

We study the kinematical properties of galaxies in the Epoch of Reionization via the [C II]158 μm line emission. The line profile provides information on the kinematics as well as structural properties such as the presence of a disc and satellites. To understand how these properties are encoded in the line profile, first we develop analytical models from which we identify disc inclination and gas turbulent motions as the key parameters affecting the line profile. To gain further insights, we use 'Althæa', a highly resolved (30 pc) simulated prototypical Lyman-break galaxy, in the redshift range $z = 6$–7, when the galaxy is in a very active assembling phase. Based on morphology, we select three main dynamical stages: (I) merger, (II) spiral disc, and (III) disturbed disc. We identify spectral signatures of merger events, spiral arms, and extra-planar flows in (I), (II), and (III), respectively. We derive a generalized dynamical mass versus [C II]-line FWHM relation. If precise information on the galaxy inclination is (not) available, the returned mass estimate is accurate within a factor 2 (4). A Tully–Fisher relation is found for the observed high-z galaxies, i.e. $L_{[\mathrm{C\,II}]} \propto (\mathrm{FWHM})^{1.80 \pm 0.35}$ for which we provide a simple, physically based interpretation. Finally, we perform mock ALMA simulations to check the detectability of [C II]. When seen face-on, Althæa is always detected at $>5\sigma$; in the edge-on case it remains undetected because the larger intrinsic FWHM pushes the line peak flux below detection limit. This suggests that some of the reported non-detections might be due to inclination effects.

Key words: methods: analytical – methods: numerical – ISM: evolution – galaxies: evolution – galaxies: high-redshift – galaxies: kinematics and dynamics.

1 INTRODUCTION

Answering the fundamental questions related to the formation, build-up, and mass assembly of galaxies is one of the main goals of modern astrophysics. The first stars and galaxies formed when the diffuse baryonic gas in the Intergalactic Medium (IGM) was able to collapse into the potential well of the dark matter halos in the early universe. The ultraviolet (UV) radiation produced by these first sources ionized the hydrogen atoms in the surrounding IGM. This process, called cosmic reionization (Madau, Haardt & Rees 1999; Gnedin 2000; Barkana & Loeb 2001), took about 1 billion years to reach completion at $z \sim 6$ (Fan et al. 2006; McGreer, Mesinger & Fan 2011). After the formation of first sources, as time progressed, those objects gradually evolved, merging with their neighbours and accreting large quantities of gaseous fuel from a filamentary IGM. Then, through a combination of galaxy–galaxy mergers, rapid star formation, and secular evolution, the morphology of those galaxies transformed into what is observed locally. Both observationally and theoretically, understanding the details of the assembly process has proven very challenging as the internal structure of these system should be resolved.

Integral field spectroscopy and adaptive optics technology have enabled us to obtain diagnostic spectra of spatial regions resolved on scales of roughly 1 kpc at intermediate redshifts ($z \sim 2$–3). These remarkable experiments revealed that such galaxies have irregular and clumpy morphologies while their velocity structures are often consistent with rotating discs (Genzel et al. 2011; Förster Schreiber et al. 2018; Leung et al. 2019). The question remains if the situation is the same for the galaxies at even higher redshifts.

★ E-mail: mahsa.kohandel@sns.it

Published by Oxford University Press on behalf of the Royal Astronomical Society

Over the last few years, observations have also managed to probe galaxies at progressively higher redshifts (for a recent review see Dayal & Ferrara 2018), producing a first, albeit partial, census of galaxy populations well into the Epoch of Reionization (EoR). Although with UV surveys (e.g. Smit et al. 2014; Bouwens et al. 2015) the discovery of such galaxies has become possible, physical insights on the properties of the interstellar medium (ISM) of these sources rely on the detection of far-infrared (FIR) lines. It has now become possible with the advent of the Atacama Large Millimeter Array (ALMA) to detect these emission lines from high-z galaxies.

Among the FIR lines, the fine-structure transition $2P_{3/2} \rightarrow 2P_{1/2}$ of singly ionised carbon at $\lambda = 158\mu$m is the brightest one, accounting for 0.1 per cent to 1 per cent of the total FIR luminosity (Stacey et al. 1991), making it as one of the most efficient coolants of the ISM (Malhotra et al. 1997; Luhman et al. 1998, 2003). Neutral carbon has a relatively low ionization potential (11.3 eV) and its distinctive line transition ([C II]) is very easy to excite ($E/k \approx 92$ K). These properties are such that the line can arise from nearly every phase in the ISM. It can emerge from diffuse H I clouds, diffuse ionized gas, molecular gas, and from the photodissociation regions (PDRs). So far, the [C II]158 μm line has been measured in a rapidly increasing number of galaxies at $z > 6$ (e.g. Capak et al. 2015; Maiolino et al. 2015; Pentericci et al. 2016; Carniani et al. 2017; Jones et al. 2017; Matthee et al. 2017; Carniani et al. 2018a,b; Smit et al. 2018).

Alongside observations, theoretical attempts have been made to model the [C II] emission and interpret the observations at $z > 6$ (Vallini et al. 2013, 2015; Olsen et al. 2017;Pallottini et al. 2017a; Katz et al. 2019) using numerical simulations of galaxies. So far, the purpose of theoretical modellings was mostly to estimate the total [C II] luminosity of galaxies at the EoR and understanding the relative contribution from different ISM phases. These theoretical works agree on the fact that most of the total [C II] luminosity arises from the dense PDRs (Pallottini et al. 2017a) with a slight dependence on galaxy mass (Olsen et al. 2017). Still no clear consensus has been reached whether or not the local [C II] star formation rate (SFR) relation that is observed locally (De Looze et al. 2014) holds for $z > 6$ galaxies (cfr Carniani et al. 2018a). For instance while Vallini et al. (2015) and Pallottini et al. (2017a) show that a deviation is present, Katz et al. (2019) show that for their suite of simulations at $z \sim 9$, the local relation holds. The [C II]–SFR relation is further analysed in different works (Ferrara et al. in preparation; Pallottini et al. 2019), where it is connected to galaxy evolutionary properties.

With the improvement of the quality of the view that ALMA is giving us from the high-z universe, the [C II] line is starting to be considered as a suitable tool for studying the gas kinematics as well. For instance, Smit et al. (2018) recently presented [C II] observations of two galaxies at $z \sim 7$ characterized by velocity gradients consistent with undisturbed rotating gas discs. Also in Jones et al. (2017), using the [C II] line emission from a $z \sim 6$ Lyman break galaxy, conjectured that their observed system represents the early formation of a galaxy through the accretion of smaller satellite galaxies along a filamentary structure. However, the build-up process, kinematics, and morphology of these galaxies are almost uncharted territories. Also, whether a disc structure is expected at those early epochs and whether it can survive the frequent collisions with merging satellites and accreting streams are key questions for galaxy formation theories.

In this work, we explore these questions by modelling the spectral profile of the [C II] emission coming from galaxies at $z > 6$. To this aim, we first construct a simple galaxy model with controllable parameters and study the emerging [C II] spectra. Then, we trace the evolution of a prototypical Lyman Break Galaxy (LBG) – 'Althæa' (Pallottini et al. 2017b) – from $z = 7$ to $z = 6$ through its [C II] emission maps and corresponding synthetic spectral line profiles.

The paper is organized as follows. In Section 2, we detail the emission model used throughout the paper, in particular analysing the effects of various assumptions made; this is followed by the description of our analytical galaxy model (Section 3) and the corresponding results. Then in Section 4, the description of the hydrodynamical simulation used in this work is given, along with the results obtained by combining it with our emission model. Then in Section 5, we compare our findings with the available [C II] observations. Finally, conclusions are summarized in Section 6.

2 [C II] EMISSION MODEL

The [C II] transition can be excited via collisions of singly ionized carbon atoms (C II) with other species present in the gas. Following Dalgarno & McCray (1972), we consider a partially ionized volume of gas in which carbon atoms are maintained in C II stage by far UV radiation in the Habing band ($6 < h\nu/\mathrm{eV} < 13.6$; Habing 1968). The [C II] emissivity (ϵ), excited by collisions with free electrons and hydrogen atoms, is written as a function of the gas (n), electron (n_e), and neutral hydrogen (n_H) number densities as follows:

$$\epsilon(n, T) = n\,(\frac{Z}{\mathrm{Z}_\odot})\,A_\mathrm{C}\left[\frac{n_\mathrm{H}}{1 + n_\mathrm{H}/n_\mathrm{H}^\mathrm{cr}}\Lambda^{2\mathrm{H}} + \frac{n_\mathrm{e}}{1 + n_\mathrm{e}/n_\mathrm{e}^\mathrm{cr}}\Lambda^\mathrm{e}\right], \quad (1)$$

where $\Lambda^\mathrm{H} = \Lambda^\mathrm{H}(T)$ and $\Lambda^\mathrm{e} = \Lambda^\mathrm{e}(T)$ are the specific cooling rates due to collision with H atoms and free electrons at temperature T. Z is the metallicity of the gas, $\mathrm{Z}_\odot = 0.0134$ is the solar metallicity (Asplund et al. 2009), and $A_\mathrm{C} = 2.69 \times 10^{-4}$ is the adopted solar ratio of carbon to hydrogen number densities (Asplund et al. 2009). Note that we have included in an approximate manner the effects of the critical density $n_\mathrm{H}^\mathrm{cr} = 3000\,\mathrm{cm}^{-3}$ and $n_\mathrm{e}^\mathrm{cr} = 8\,\mathrm{cm}^{-3}$ (Goldsmith et al. 2012) for hydrogen and electron collisions to ensure the validity of equation (1) in high-density regimes.[1]

We require ϵ to vanish in highly ionized regions ($T > 10^4$ K) where our assumption that all the carbon is singly ionized would not be valid anymore. In this treatment, we also assume that the [C II] line is optically thin (see discussion in Goldsmith et al. 2012), which means that the integrated intensity is proportional to the C II column density along the line of sight (l.o.s.), irrespective of the optical depth of the medium (see also Section 4.1). In this approximation, for each gas parcel of volume V, we then compute the [C II] luminosity as $L = \epsilon V$.

2.1 CMB effects

The cosmic microwave background (CMB) has a thermal black body spectrum at a local temperature of $T^0_\mathrm{CMB} = 2.725$ K, increasing with redshift as $T_\mathrm{CMB}(z) = (1 + z)\,T^0_\mathrm{CMB}$. Assuming local thermal equilibrium, this sets the minimum temperature of the ISM, which at high redshift becomes non-negligible. Any emission coming from the ISM will be seen against the CMB background. As discussed

---

[1] For each type of collision partner, the critical density n_cr is defined by the collisional de-excitation rate being equal to the effective spontaneous decay rate. If the density is well below n_cr, one can use the Dalgarno & McCray (1972) definition for cooling rate as the product of singly ionised carbon density with hydrogen/electron number density.

in Da Cunha et al. (2013), the contrast of the emission against the CMB radiation in the rest-frame is given by:

$$\Delta I_\nu = [B_\nu(T_\mathrm{s}) - B_\nu(T_\mathrm{CMB})]\left(1 - \mathrm{e}^{-\tau}\right), \tag{2}$$

where $B(\nu)$ is the Planck function and T_s is the spin temperature of the FIR line. Assuming the [C II] line to be optically thin in the sub-mm band, i.e. $\mathrm{e}^{-\tau_\nu} \approx 1 - \tau_\nu$, the ratio between the flux observed against the CMB and the intrinsic flux emitted will be[2]:

$$\eta \equiv \frac{F^\mathrm{obs}_{\nu/(1+z)}}{F^\mathrm{int}_{\nu/(1+z)}} = 1 - \frac{B_\nu(T_\mathrm{CMB})}{B_\nu(T_\mathrm{s})}. \tag{3}$$

As T_s approaches T_CMB, $\eta \to 0$; in this case the CMB completely suppresses the line flux. For [C II], the spin temperature is defined using the ratio of the thermal equilibrium population of the upper (u: $2_{P_{3/2}}$), and lower (l: $2_{P_{1/2}}$) level of fine structure transition:

$$\frac{n_\mathrm{u}}{n_\mathrm{l}} = \frac{g_\mathrm{u}}{g_\mathrm{l}}\mathrm{e}^{-T_*/T_\mathrm{s}}, \tag{4}$$

where $T_* = 91.7\,\mathrm{K}$ is the equivalent temperature of the level transition, and $g_\mathrm{u} = 4$, $g_\mathrm{l} = 2$ are the statistical weights. Following the procedure used in Vallini et al. (2015) (see also Pallottini et al. 2015), T_s is defined as:

$$\frac{T_*}{T_\mathrm{s}} = \ln \frac{A_\mathrm{ul}(1 + \frac{c^2 I_\nu}{2h\nu}) + n_\mathrm{e} C^\mathrm{e}_\mathrm{ul} + n_\mathrm{H} C^\mathrm{H}_\mathrm{ul}}{A_\mathrm{ul}(\frac{c^2 I_\nu}{2h\nu^3}) + n_\mathrm{e} C^\mathrm{e}_{ul}\mathrm{e}^{-T_*/T} + n_\mathrm{H} C^{H}_\mathrm{ul}\mathrm{e}^{-T_*/T}}, \tag{5}$$

where A_ul is the Einstein coefficient for spontaneous emission and C^e_ul (C^H_ul) is the collisional de-excitation rate for collisions with e (H-atoms). For the [C II] line emission $A_\mathrm{ul} = 2.36 \times 10^{-6}\,\mathrm{s}^{-1}$ (Suginohara, Suginohara & Spergel 1999) and $C^\mathrm{e}_\mathrm{lu}(T) = (8.63 \times 10^{-6}/g_\mathrm{l}\sqrt{T})\gamma_\mathrm{lu}(T)\mathrm{e}^{-T_*/T}$ with $\gamma_\mathrm{lu}(T)$ being the effective collision strength computed based on Keenan et al. (1986). $C^\mathrm{H}_\mathrm{lu}(T)$ is tabulated in Dalgarno & McCray (1972).

As discussed in Gong et al. (2012), at high redshifts the soft UV background at 1330 Å produced by the first galaxies and quasars can pump the C II ions from the energy level $2\mathrm{s}^2 2\mathrm{p}\ 2\mathrm{P}_{1/2}$ to $2\mathrm{s}2\mathrm{p}^2\ 2\mathrm{D}_{3/2}$ ($\lambda = 1334.53$ Å), and $2\mathrm{s}^2 2\mathrm{p}\ 2\mathrm{P}_{3/2}$ to $2\mathrm{s}^2 2\mathrm{p}^2\ 2\mathrm{D}_{3/2}$ ($\lambda = 1335.66$ Å). This pumping effect can lead to the [C II] transition $2\mathrm{D}_{3/2} \to 2\mathrm{P}_{3/2} \to 2\mathrm{P}_{1/2}$ which would mix the levels of the [C II] line. Similarly to Vallini et al. (2015), we add this UV pumping effect in equation (5).

To summarize, with n_e, n_H, and T we can compute the spin temperature of [C II] line using equation (5) and the CMB suppression using equation (3). In Fig. 1, the CMB suppression factor, η, is shown as a function of gas density for different temperatures and for $z = 6$. We fix the metallicity to be $Z = 0.5\,\mathrm{Z}_\odot$ and vary the temperature.[3] The cooler the gas, the more the [C II] emission is suppressed. Note that, independently of T, the emission is suppressed by about 90 per cent for low-density gas ($n \lesssim 1\,\mathrm{cm}^{-3}$), because collisions are not efficient enough to decouple T_s from the temperature of the CMB, in agreement with results in the literature (Gong et al. 2012; Pallottini et al. 2015; Vallini et al. 2015).

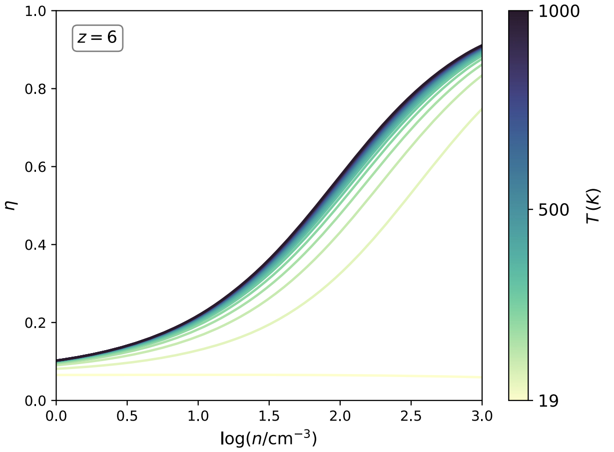

Figure 1. CMB suppression of [C II] emission (η) as a function of gas number density (n). Different lines indicate different gas temperature (T). The suppression is calculated at redshift $z = 6$ via equation (3); see the text for the details of the calculation.

3 SEMI-ANALYTICAL INSIGHTS

We start by developing a simple analytical model of a disc galaxy to elucidate the physics involved in shaping the line profile, and to build a controlled environment for the analysis of [C II] emission from high-z galaxies. We consider a geometrically thin disc and assume that the surface brightness profile of the disc has an exponential form:

$$I(r) \propto \exp(-r/r_\mathrm{d}), \tag{6}$$

where r_d is the disc scale length. If the mass surface density is also exponential with the same scale length, i.e.:

$$\Sigma(r) = \Sigma_0 \exp(-r/r_\mathrm{d}), \tag{7}$$

the potential that such a disc would generate at the equatorial plane is (Binney & Tremaine 2008):

$$\Phi(r, 0) = -\pi G \Sigma_0 r[I_0(y)K_1(y) - I_1(y)K_0(y)], \tag{8}$$

where $y = r/2r_\mathrm{d}$ and I_n, K_n are the modified Bessel functions of first and second kind, respectively. If we differentiate this potential with respect to r, we obtain the circular speed of the exponential disc (Freeman 1970):

$$v^2_\mathrm{c}(r) = 4\pi G \Sigma_0 r_\mathrm{d} y^2 [I_0(y)K_0(y) - I_1(y)K_1(y)]. \tag{9}$$

Using the circular velocity v_c, we can define the velocity along the l.o.s. as follows:

$$v(r, \theta, \phi)^2 = 4\pi G \Sigma_0 r_\mathrm{d} y^2 [I_0(y)K_0(y) - I_1(y)K_1(y)] \cos^2\phi \sin^2\theta, \tag{10}$$

where θ is the angle between the l.o.s axis and the normal to the disc plane and ϕ is the polar angle on the plane of the face-on disc. We assume a thin disc with $\Sigma_0 = 1000\,\mathrm{M}_\odot/\mathrm{pc}^2$, $r_\mathrm{d} = 3\,\mathrm{kpc}$, and a thickness of 100 pc.

For our kinematic analysis, it is useful to define a 2D Cartesian grid centred on the galaxy centre. We choose a grid of size $(24\,\mathrm{kpc})^2$ divided in a total of $(4 \times 10^3)^2$ cells, i.e. each cell has a linear resolution of 6 pc. In each cell, surface density and velocities are computed using equations (7) and (10), respectively. We also account for random turbulent motions (i.e. deviations from perfect circular orbits) by adding in each cell a random velocity, the

---

[2] FIR flux observed against CMB is defined as $F^\mathrm{obs}_{\nu/(1+z)} = (1+z)A\Delta I_\nu/d^2_\mathrm{L}$, where A is the physical area of the galaxy and d_L is the luminosity distance.

[3] In this case, the ionization fraction of the gas is computed by solving the equilibrium between collisional ionisation, ionization due to cosmic rays and X-rays and recombination rates for H and He (Wolfire et al. 1995). It depends on hydrogen number density, temperature, and metallicity of the gas.

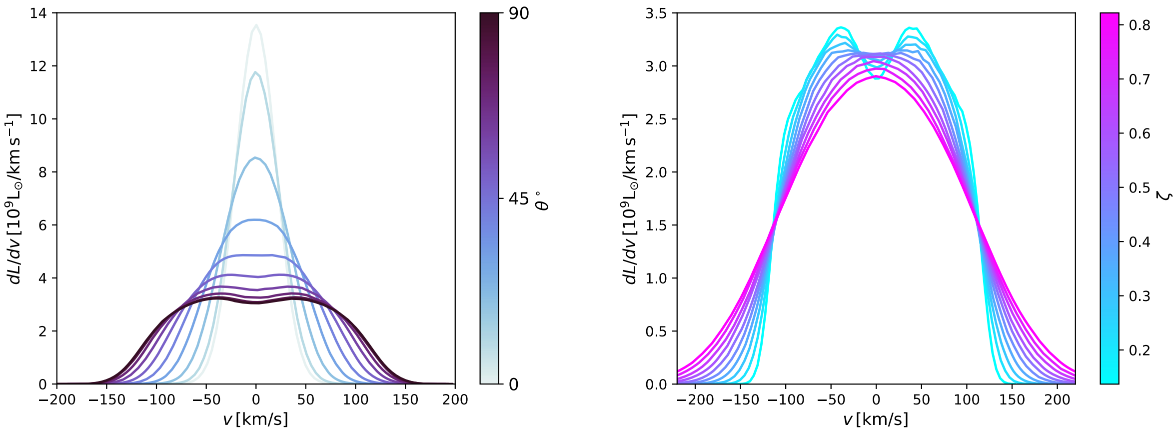

Figure 2. Spectral profile of a geometrically thin disc with an exponential profile. Left-hand panel: Disc inclination is between $\theta = 0^\circ$ (face-on) and $\theta = 90^\circ$ (edge-on). In addition to rotational velocities, isotropic turbulent motions extracted from a Gaussian distribution having an r.m.s. amplitude of $20\,\mathrm{km\,s^{-1}}$ are added to the disc. Right-hand panel: The inclination of the disc is fixed to be edge-on and we vary the amplitude of turbulent motions. Both inclination and large turbulent motions broaden the wings of the line and lower the amplitude by a factor of 4 and 1.2, respectively.

components (t) of which are extracted from a Gaussian distribution:

$$p(t) = \frac{1}{\sqrt{2\pi\, {v_t}^2}} \mathrm{e}^{-t^2/2v_t^2}, \tag{11}$$

where v_t is the standard deviation of the distribution. We further assume isotropic turbulence so the three added components have the same magnitude.

Assuming a uniform temperature of $100\,\mathrm{K}$[4] for the disc, an ionisation fraction of $x_\mathrm{e} = 0.2$, and a metallicity of $Z = \mathrm{Z}_\odot$, we compute the [C II] luminosity using the model described in Section 2. Having the l.o.s velocity and luminosity for each cell, we extract the integrated spectral profile by computing the histogram of velocities weighted by the corresponding value of [C II] luminosity.

First, we explore the effect of inclination of the disc by focusing on the spectral profile of the emission. In the left-hand panel of Fig. 2, we show the [C II] spectra from our disc galaxies including turbulent velocities with $v_\mathrm{t} = 20\,\mathrm{km\,s^{-1}}$. Different lines correspond to a different inclination of the disc. As discussed by Elitzur, Asensio Ramos & Ceccarelli (2012), the spectral profile of such a disc in the edge-on view ($\theta = 90^\circ$) should show a double peak structure. We see in Fig. 2 that inclining the disc from face-on view ($\theta = 0$) to the edge-on one smoothly changes the spectral profile from having a Gaussian shape to the double peak structure. Also inclining the disc towards edge-on produces broader wings compared to the face-on case. In addition, the peak amplitude of the line decreases by factor of 4 in the edge-on case. These effects happen because by inclining the disc towards the edge-on view, $\sin(\theta) \to 1$ (see equation 10) allows for stronger contributions from high l.o.s. velocities. Consequently, the peak amplitude of the line decreases to keep the total [C II] luminosity, given by the integral below the curve, constant.

Random motions also change the spectral profile. In the right-hand panel of Fig. 2, we set the inclination of the disc to be edge-on (double peak profile) and then vary v_t. For each of the cases with different turbulence velocities, we calculate $\zeta = v_t/\bar{v}_\mathrm{c}$ in which $\bar{v}_\mathrm{c} \simeq 75\,\mathrm{km\,s^{-1}}$ is the mass-weighted average circular velocity of the exponential disc. We find (Fig. 2, right-hand panel) that if $\zeta > 0.5$ the double peak profile is erased, which means that turbulent motions can mask the presence of the disc in the spectrum. Furthermore, and similarly to the effect of inclination discussed above, turbulence broadens the line wings and decreases the line intensity at the peak by a factor of 1.2.

With these controlled case examples, we conclude that depending on the inclination of the disc and the amount of turbulent motions, emission from a rotating disc might produce quite a range of different line profiles. In particular, inclination and turbulence have a degenerate effect in changing the spectral shape of emission. The double peak signature of our rotating edge-on disc is erased either by changing the inclination ($\theta < 70^\circ$) or significant turbulent velocities ($\zeta > 0.5$). Similarly, the single Gaussian shape can be the signature of a highly turbulent disc or simply a face-on view of a disc with moderate turbulent motions.

Here, for a better comparison with the following analysis of the simulation (Section 4), it is convenient to define two cases of our analytical model; smooth disc: a smooth disc with $\zeta < 0.5$ featuring a symmetric double-peak profile in the edge-on view and a single Gaussian profile in the face-on view and turbulent-dominated disc: a disturbed disc with $\zeta > 0.5$, which has a smooth single Gaussian spectral profile both in the face-on and edge-on view.

4 HIGH-REDSHIFT GALAXY SIMULATIONS

We now turn our analysis to the more realistic case of galaxies extracted from zoom-in cosmological simulations, whose main features are outlined below. This is a necessary step to produce reliable predictions that catch the ISM complexity during galaxy assembly and thus can be directly confronted with observational data. For details of the simulation, we refer the reader to Pallottini et al. (2017b).

Pallottini et al. (2017b) uses a customized version of the adaptive mesh refinement code RAMSES (Teyssier 2002) to zoom-in on the evolution of 'Althæa', a $z \sim 6$ LBG hosted by a dark matter halo of mass $\simeq 10^{11}\mathrm{M}_\odot$. The gas mass resolution of the zoom-in region in this simulation is $1.2 \times 10^4\ \mathrm{M}_\odot$ and the additional adaptive refinement allows us to resolve spatial scales down to $\simeq 30\,\mathrm{pc}$ at $z \sim 6$. In this simulation, a non-equilibrium chemical

---

[4] The reference temperature $T = 100$ K is the mean temperature found for molecular gas in our high-z galaxies simulations, see Fig. 8 in Pallottini et al. (2017b).

network has been implemented via the code KROME (Grassi et al. 2014) which includes H, H^+, H^-, He, He^+, He^{++}, H_2, H_2^+, and electrons (see also Bovino et al. 2016). Stars are formed according to the Kennicutt–Schmidt relation (Schmidt 1959; Kennicutt 1998) that depends on the molecular hydrogen density computed from the non-equilibrium chemical network. As described in Pallottini et al. (2017a), stellar feedback includes supernovae, winds from massive stars, and radiation pressure. It also accounts for the blast wave evolution inside molecular clouds. The thermal and turbulent energy content of the gas is modelled similarly to Agertz & Kravtsov (2015).

At $z = 6$, Althæa is characterized by a stellar mass $M_\star \sim 10^{10} \mathrm{M}_\odot$ and SFR $\sim 100\,\mathrm{M}_\odot \mathrm{yr}^{-1}$. During its evolution, the SFR-stellar mass relation of Althæa is comparable to what is inferred from high-z observations (Jiang et al. 2016). By modelling the internal structure of molecular clouds, Vallini et al. (2018) used Althæa to predict the CO line emission. By post-processing the simulation with radiation transfer through dust Behrens et al. (2018) were able to reproduce the observed properties of A2744_YD4 (Laporte et al. 2017), one of the most distant ($z \approx 8.3$) galaxies where dust continuum is detected.

In this work, we are interested in studying the evolution of Althæa from $z = 7$ to $z = 6$ in its integrated [C II] surface brightness (luminosity), and the corresponding spectra along different l.o.s. identified by $\hat{n}$. Our aim is to investigate different kinematical features and their connection with the assembly process as imprinted in the [C II] line profile.

4.1 Computing [C II] maps and spectra

The first step is to compute the [C II] luminosity. For that, we need n, n_{H}, n_{e}, T, and Z as the inputs for the emission model (equation 1) and CMB suppression (equation 3). The first three parameters are computed by the simulation on-the-fly via the chemical network included in KROME. Temperature in RAMSES is defined from the thermal pressure and the gas density ($\rho = \mu m_{\mathrm{H}} n$, where μ and m_{H} are the mean molecular weight and the hydrogen atom mass, respectively) by assuming an equation of state, i.e. $T = (\gamma - 1)\, P_{\mathrm{k}}/\rho$, with $\gamma = 5/3$ being the adiabatic index.

To derive the spectrum, in addition to the above mentioned quantities, we need to know the l.o.s. velocity for each cell, namely $v_i = \vec{V}_i \cdot \hat{n}$, where $\vec{V}_i$ is the simulated velocity field of the galaxy and $\hat{n}$ the l.o.s. direction. Having these quantities, we model the contribution of each simulated ith cell to the spectrum as a Gaussian function centred on v_i with a width $\sigma^i_{\mathrm{k,t}}$ and an amplitude equal to the [C II] luminosity (L^i_{CII}) of that cell. $\sigma^i_{\mathrm{k,t}}$ is the broadening of the line for which we account for both the thermal and the turbulent motions as $\sigma^i_{\mathrm{k,t}} = \sqrt{(P^i_{\mathrm{k}} + P^i_{\mathrm{t}})/\rho_i}$, where P^i_t is the pressure due to the turbulent motions induced by the kinetic feedback in the simulation. For each velocity bin v_j we compute the integrated line spectrum $f_j = f_j(v_j)$ as:

$$f_j = \sum_i \frac{L^i_{\mathrm{CII}}}{2\sqrt{\pi}\sigma^i_{\mathrm{k,t}}} \mathrm{e}^{-\left[(v_i - v_j)/\sqrt{2}\sigma^i_{\mathrm{k,t}}\right]^2}. \qquad (12)$$

Having the spectrum as a function of the velocity bin, we define the mean spectral velocity as:

$$\langle v \rangle = \frac{\sum_j v_j f_j}{\sum_j f_j}, \qquad (13)$$

which we use to centre the velocities in plotting the spectra. We compute the full width at half-maximum (FWHM) of the line as the full width at which 68 per cent of the light is contained.; note that in calculating FWHM we do not consider values of f_j lower than 10 times the peak of the flux.

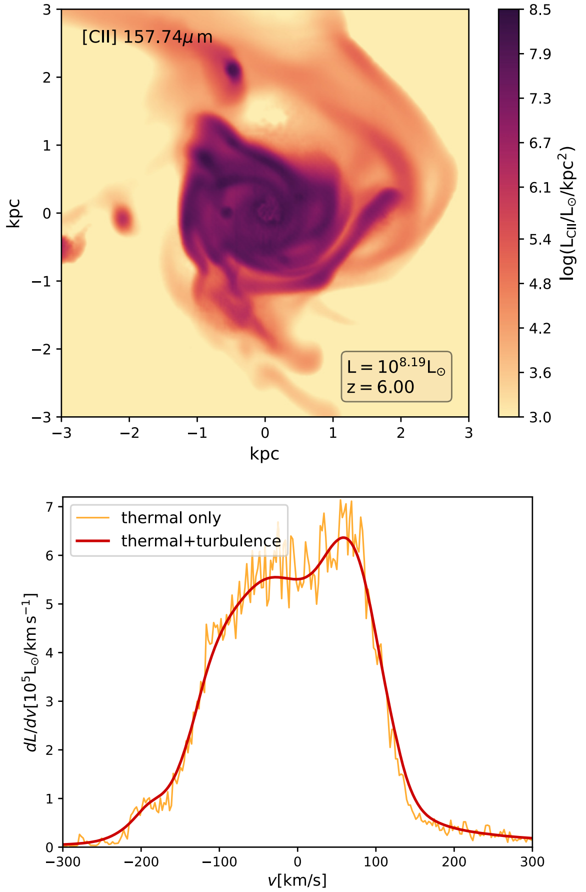

Figure 3. Top panel: Surface brightness of [C II] emission of Althæa (viewing face-on) at redshift $z = 6$. Bottom panel: The corresponding synthetic [C II] spectral profile. The spectrum either includes (red line) or does not include (yellow) turbulent broadening; in the latter case, only thermal broadening is taken into account. Turbulent motions smooth out the spectrum by erasing the spiky behaviour and decreasing the line intensity at the peak by 10 per cent. The total spectrum shows two comparable peaks of emission with a relative difference of < 15 per cent.

Note that throughout this paper the [C II] maps are calculated by accounting for the emission of the gas centred on the simulated galaxy that is within a cube with side equal to the field of view (FOV) of the image. Unless noted otherwise, the spectra corresponding to a map are extracted from the same FOV.

4.2 An example of [C II] surface brightness and spectrum

We start by discussing the properties of [C II] emission coming from the face-on[5] view of Althæa at $z = 6$ in a rectangular FOV of size 7 kpc around the centre of the galaxy. In Fig. 3, we plot the l.o.s.-integrated surface brightness of the galaxy at this stage. The total [C II] luminosity is $L_{[\mathrm{CII}]} = 10^{8.19} \mathrm{L}_\odot$. The galaxy shows a relatively smooth disc-like structure, whose extent is 2 kpc in [C II] emission. At this redshift, this translates to an angular size of

---

[5] With face-on we mean that we orient the l.o.s. parallel to the eigenvector of the inertia tensor of the gas density distribution with the largest eigenvalue.

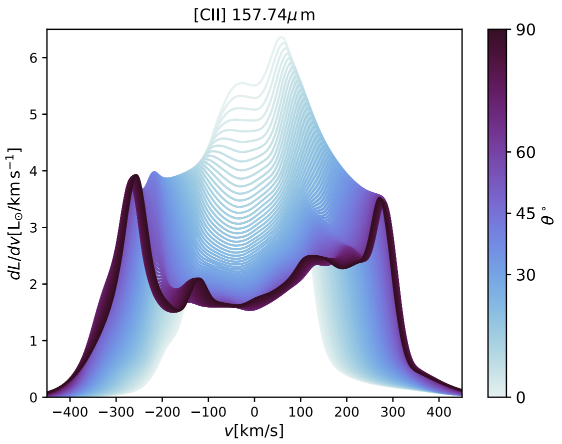

Figure 4. Synthetic spectra for Althæa at $z = 6$ (see also Fig. 3). Spectra are calculated for 100 inclinations between face-on ($\theta = 0^\circ$) and edge-on ($\theta = 90^\circ$) views. Changing the inclination clears the signature of rotating disc from the spectral shape, i.e. the two comparable peaks at the edges. From face-on to edge-on the peak amplitude of the line decreases by a factor of 1.6.

0.34 arcsec. For these early epochs, there is a clear hint of a broken spiral arm structure. The other interesting feature is the presence of bright clumps of size ≈100 pc within the disc.

Also shown in Fig. 3 is the corresponding synthetic face-on [C II] line spectrum; for comparison, we also present the spectrum in which only thermal broadening is taken into account. The main effect of the inclusion of turbulent motions, self-consistently derived from the simulation in each cell, is to make the line profile smoother by erasing the narrow spikes visible in the thermal-only broadened profile. As seen in the analytical model (Section 3), turbulent motions[6] can suppress characteristic features of the spectrum, such as the double-peak profile of a rotating disc. Note that the maximum of the rotational velocity of the galaxy is of order ∼190 km s^{-1} (see also in Fig. 7), while the level of turbulence for dense gas is of order of $\sigma_t \simeq 30$ km s^{-1} (Vallini et al. 2018); thus the effect of micro-turbulence is limited with respect to the range of turbulence explored in the analytical model. Accounting for turbulent motions in Althæa decreases the line intensity at the peak by 10 per cent, as it was expected from the analytical model.

As pointed out in Section 3, a decreasing inclination can erase the signatures of a disc in the spectra, similar to what happens when increasing turbulent motions. To investigate the situation in our simulated galaxy, we extract [C II] spectra for 100 inclinations between the face-on and the edge-on view of Althæa disc at $z = 6$ and we plot the result in Fig. 4. Surprisingly, there are two comparable peaks in the spectrum when Althæa is seen edge-on. This confirms that the gas in the ISM of this galaxy has already undergone ordered rotation at such a high redshift. As expected from our analytical model (see Fig. 2), changing the inclination of the disc washes out the signature of the rotating disc from the spectral profile. Changing the inclination of the disc from $\theta = 0^\circ$ to $\theta = 90^\circ$, the peak amplitude of the line decreases by a factor of 1.6. With respect to the analytical disc, spectral profiles contain complicated structures which are due to the asymmetries and clumpy structure of the [C II] emitting gas. The degeneracy between inclination and turbulent motions is also present in the case of simulated disc but it is more complicated (explored in the analytical model, Fig. 2). Inclining the disc towards face-on not only masks the spectral signature of the disc but also affects the appearance or disappearance of various bumps and structures in the profile.

4.3 Galaxy evolution traced by [C II]

With the tools in hand (emission maps and spectra), now we concentrate on studying the evolution of Althæa in a redshift range of $6.09 < z < 7$ (corresponding to a time span of 183 Myr) when the system is in a very active assembling phase. In Fig. 5, we show the face-on emission maps of Althæa in that redshift range. The time lapse among different panels is 1 Myr and the images are taken in a FOV of 7 kpc. At the earliest epochs, the galaxy is constituted by a small (500 pc) disc surrounded by several emission knots of size < 100 pc, which are feeding the central part through filaments. As time progresses, the disc grows in size and mass in an inside-out fashion, forming a compact core while acquiring mass from the satellites which are progressively disrupted and embedded in the disc. At $z = 6.48$, a merger event occurs, which is clearly seen in Fig. 5. The merger event dramatically perturbs the quasi-smooth disc structure, resulting in the very irregular and widespread emission seen at $z = 6.38$. However, the gravitational potential of the galaxy is able to restore the disc in less than 16 Myr.

Among these stages, we select three particularly interesting stages for further analysis based on their [C II] emission morphology:

Merger: At $z = 6.48$, when Althæa experiences a merger event. The satellite in this stage has no stars but is hosted in a dark matter sub-halo that is about to merge with the galaxy. The total [C II] luminosity at this stage is $10^{7.87}$L$_\odot$.

Spiral disc: At $z = 6.28$, the ISM of Althæa has relaxed into a disc which has a spiral arm in one side. The total [C II] luminosity at this stage is $10^{7.71}$L$_\odot$.

Disturbed disc: This stage corresponds to $z = 6.18$ in which disc has been vertically disrupted. The total [C II] luminosity at this stage is $10^{7.86}$L$_\odot$.

In the two middle panels of Fig. 6, [C II] images for the face-on and edge-on views of the above selected stages are shown. These stages are selected because they have distinct differences in morphology and structure which in principle can evoke differences in the spectral profile of the emission. Furthermore, we plot the l.o.s. velocity profiles of these stages in Fig. 7. These profiles are not monotonic and contain several bumps and peaks. This is an indication of the complex velocity structure of the gas. In the following, we compare these stages of the simulation with each other and also with the cases defined in our analytical model in terms of their spectral profile.

Recall from the analytical model that a double-peak profile is a signature of having a rotating disc in the system while a single peak Gaussian profile can be a signature of either a disturbed disc or a face-on view of a rotating disc (Section 3). We apply the spectra diagnostic to the face-on and edge-on views of the above defined stages. As visible in the [C II] images, multiple structures

---

[6] Note that, the turbulence is defined differently in the simulation and the analytical model. In the analytical disc, every motion but the circular ones are treated as turbulence, while in simulation, turbulence is present because of the kinetic feedback. To make an exact comparison, one should fit a disc model to the simulated galaxy and then define the turbulence as it is in the analytical model.

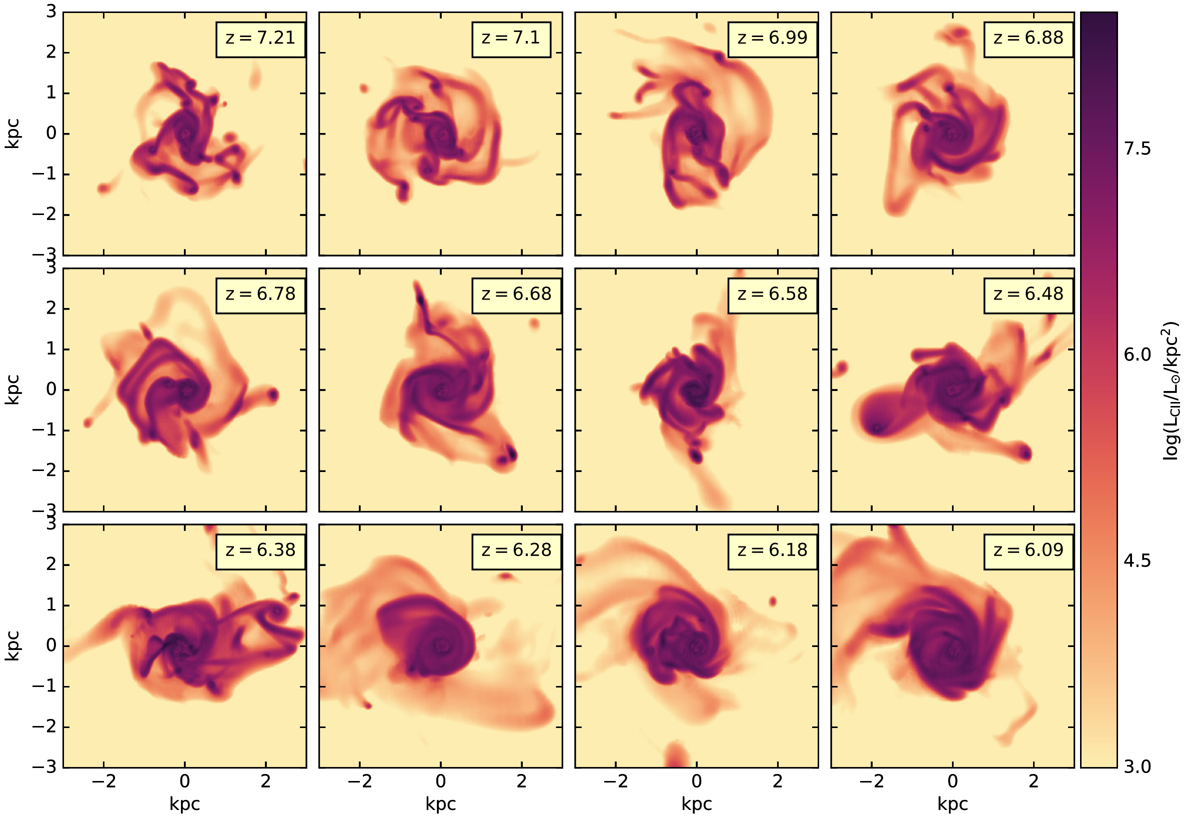

Figure 5. [C II] surface brightness of Althæa during its evolution in redshift range of $6.09 < z < 7$. Time is increasing from left to right, top to bottom. Neighbouring panels are separated by 16 Myr.

are present in the ISM of these systems, beyond the central 2 kpc. To distinguish between the central disc and the environment of the system, we extract the spectra for each of the stages in two FOV sizes, 7 kpc and 2 kpc. In the left-hand panels of Fig. 6, these spectra for the face-on view of the stages are plotted, while in the right-hand panels the spectra for the edge-on views are plotted.

The profile of the face-on view of all the stages contain a dominant single peak but they are different in comparison to smooth disc and turbulent dominated disc defined in the semi-analytical model.

The face-on profile of the merger stage has an FWHM $= 167\,\mathrm{km\,s^{-1}}$ and the profile shows two merged peaks located at $v = -100\,\mathrm{km\,s^{-1}}$ and $v = 0\mathrm{km\,s^{-1}}$; the major peak is due to the central disc while the addition of [C II] from the starless satellite produces the secondary peak in the profile. The face-on view of the spiral disc with an asymmetric Gaussian shape has an FWHM $= 100\,\mathrm{km\,s^{-1}}$ and peak flux of 0.35mJy. The asymmetry of the profile reflects the asymmetric kinematics of the [C II] emitting gas. Instead the spectral profile of the disturbed disc in face-on view is semisymmetric but it is wider (FWHM $= 143\,\mathrm{km\,s^{-1}}$) in the core because of the extra-planar flows perpendicular to the disc plane; such extra-planar flows can contribute to 10 per cent of the total signal, as it is analysed in Gallerani et al. (2018).

In summary, the presence of broken spiral arm, extra-planar flows and a merging satellite encode spectral signatures as asymmetric Gaussian peaks in the profile, broadening the core of the spectrum and a quite dominant peak very close to the disc's main peak in the face-on spectral profiles respectively.

We perform a similar comparison for the edge-on spectra. The situation for the edge-on profiles is more complicated because the spectra of the simulated stages are very structured. The edge-on profile of the merger stage (with peak of 0.14 mJy) contains dominant asymmetric double-peaks (with relative difference of 18 per cent) because of the presence of the central rotating disc. Various bumps are present in the total spectrum and the most prominent one is due to the satellite: its magnitude is comparable to that of the horns of the disc, it is centred around $v = +100\,\mathrm{km\,s^{-1}}$ and has a velocity extension of $300\,\mathrm{km\,s^{-1}}$. Since this stage shows a clear hint of rotation in the spectrum, it implies that distinguishing systems with close mergers from a rotating system is very difficult using only spectra (Simons et al. 2019).

For the spiral disc, the total spectrum has a peak flux of 0.12 mJy and FWHM $\sim 479\,\mathrm{km\,s^{-1}}$; from the spectral shape, there is a clear hint of rotation because of the presence of double peaks in the two edges of the spectrum. The double peaks in the spectral profile are not symmetric as in the analytical model in smooth disc. This is because of the asymmetries seen in the disc of [C II] emitting gas (see the right-hand panel of Fig. 6). In addition, there is a quite prominent bump in the core of the spectrum which was not present in the profiles of the analytical disc. The bumps in the spectrum are due to external gas (> 2 kpc) flowing into the disc. In this case, the contribution of the co-planar spiral arm to the edge-on spectrum becomes more prominent making the high-velocity tails.

As it is expected from the analytical model, the edge-on profile of the simulated disturbed disc does not have rotating double peaks. However, instead of having a smooth single Gaussian profile, there is an asymmetric Gaussian profile (centred on $v = 200\mathrm{km\,s^{-1}}$) including multiple peaks in the long skewed tail. There is a relative

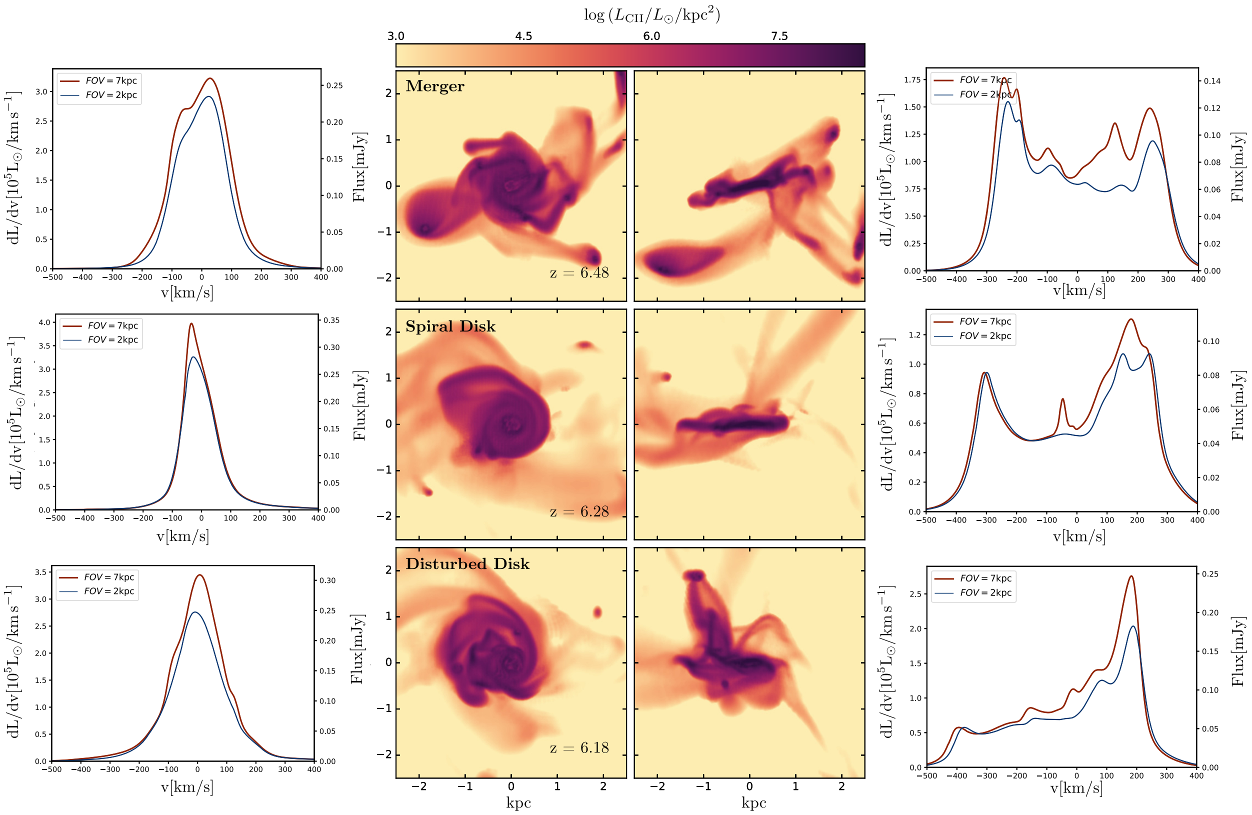

Figure 6. Left-hand panel: [C II] spectra for the face-on inclinations taken from FOV = 7 kpc (red solid lines) and FOV = 2 kpc (blue solid lines). Middle panels: Face-on and edge-on emission maps for Althæa in different representative stages of evolution: merger stage (top), spiral disc (centre), and disturbed disc (bottom). Right-hand panel: [C II] spectra for the edge-on inclinations taken from FOV = 7 kpc (red solid lines) and FOV = 2 kpc (blue solid lines).

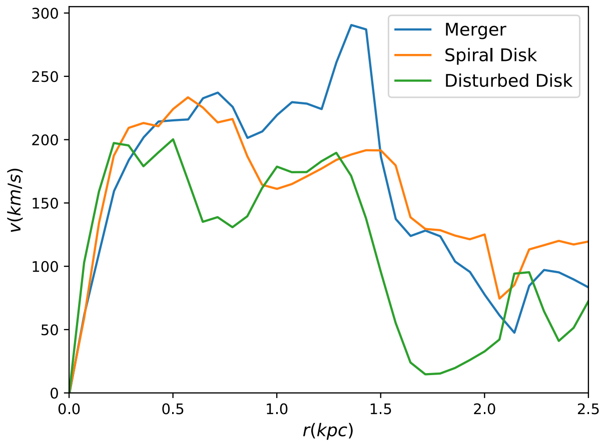

Figure 7. Velocity structure of Althæa in different evolutionary stages (see Fig. 6) in the edge-on view.

difference of 80 per cent between the main peak of the spectrum and the lowest bump in the tail. The presence of extra-planar flows suppresses the blue part of the spectrum masking the signature of rotating disc which was present in the spiral disc profile. Recall that disturbed disc stage is just 16 Myr after the spiral disc stage in the evolution of Althæa.

The spectra for the simulated galaxy are very structured and complicated. To properly interpret the component analysis, it is required to apply full dynamical studies and extract the spectra for different velocity channels of the system. This is beyond the scope of this paper and is left for future studies.

5 OBSERVATIONAL IMPLICATIONS

Investigating the evolution of Althæa, we have seen how the structural and kinematical differences result in various spectral profiles which depend on morphological properties, and inclination of the galaxy (Fig. 4). In this section, we analyse the implications of these results from an observational point of view.

For the synthetic spectra, we use the three different stages of Althæa discussed in Section 4.3. Our results are compared with observations of a sample of $5.2 < z < 7.1$ galaxies for which the spectra of [C II] line have been obtained with ALMA (Ouchi et al. 2013; Wang et al. 2013; Capak et al. 2015; Pentericci et al. 2016; Jones et al. 2017; Carniani et al. 2017). For reference, these objects are listed in Table 1, along with their redshift, total [C II] luminosity ($L_{\rm CII}$) and FWHM of the [C II] line.

5.1 Dynamical mass estimates

By assuming a rotating disc geometry (with radius R) for the [C II] emitting gas, the dynamical mass can be estimated as:

$$M_{\rm dyn} = \frac{v_{\rm c}^2 R}{G}\,. \qquad (14)$$

From a [C II] spectrum obtained with a high signal-to-noise ratio and a good sampling of the velocity channels one can estimate $v_{\rm c}$

Table 1. Sample of high-z galaxies probed by [C II] line.

Target name	ID	z	$\mathrm{Log}(L_{[\mathrm{C\,II}]}/\mathrm{L}_{\odot})$	FWHM/$\mathrm{km\,s^{-1}}$	Reference
UDS16291	U16	6.64	7.9	50	Pentericci et al. (2016)
RXJ1347:1216	RXJ	6.77	7	75	Bradač et al. (2017)
COSMOS13679	C13	7.15	7.9	90	Pentericci et al. (2016)
WMH5b	WMH5b	6.07	8.4	94	Jones et al. (2017); Willott et al. (2015)
A385-5.1	A38	6.03	6.9	100	Knudsen et al. (2016)
BDF3299	B32	7.15	7.8	102	Maiolino et al. (2015); Carniani et al. (2017)
COS-2987030247	C29	6.81	8.6	124	Smit et al. (2018)
HZ8w	HZ8W	5.15	8.3	136	Capak et al. (2015)
COSMOS24108a	C24a	6.63	7.9	150	Pentericci et al. (2016)
COSMOS24108	C24	6.63	8.1	150	Pentericci et al. (2016)
BDF2203	B22	6.12	8.1	150	Carniani et al. (2018a)
CLM1	CLM1	6.17	8.4	162	Willott et al. (2015)
HZ1	HZ1	5.69	8.4	165	Capak et al. (2015)
HIMIKO	HIMIKO	6.60	8.1	180	Ouchi et al. (2013); Carniani et al. (2018b)
HZ6	HZ6	5.29	9.2	188	Capak et al. (2015)
HZ3	HZ3	5.54	8.7	200	Capak et al. (2015)
COS-3018555981	C30	6.85	8.7	230	Smit et al. (2018)
NTTDF6345	N63	6.70	8.2	250	Pentericci et al. (2016)
WMH5	WMH5	6.07	8.7	251	Jones et al. (2017); Willott et al. (2015)
HZ8	HZ8	5.15	8.7	254	Capak et al. (2015)
WMH5a	WMH5a	6.07	8.5	270	Jones et al. (2017); Willott et al. (2015)
HZ4	HZ4	5.54	9.0	297	Capak et al. (2015)
B14-65666	B14	7.15	9.1	349	Hashimoto et al. (2018)
HZ9	HZ9	5.54	9.2	351	Capak et al. (2015)
HZ2	HZ2	5.66	9.0	377	Capak et al. (2015)
HZ7	HZ7	5.25	8.7	483	Capak et al. (2015)

from the FWHM of the line using the following expression:

$$\mathrm{FWHM} = \gamma v_{\mathrm{c}} \sin\theta, \tag{15}$$

where γ is a factor of order of unity that depends on geometry, line profile, and turbulence. Different values have been assumed in the literature for γ: for example, Capak et al. (2015) assumed $\gamma = 1.32$. Using equations (14) and (15), the general expression for the dynamical mass is:

$$\mathrm{M}^{\mathrm{est}}_{\mathrm{dyn}} = 2.35 \times 10^{9}\mathrm{M}_{\odot} \left(\frac{1}{\gamma^2 \sin^2\theta}\right) \left(\frac{\mathrm{FWHM}}{100\,\mathrm{km\,s^{-1}}}\right)^2 \left(\frac{\mathrm{R}}{\mathrm{kpc}}\right). \tag{16}$$

Before discussing the mass estimates, let us consider the FWHM of the spectra. We plot them as a function of inclination in Fig. 8. In general, the FWHM in Althæa is an increasing function of inclination and varies from a minimum of 100 $\mathrm{km\,s^{-1}}$ in the face-on case to a maximum of 480 $\mathrm{km\,s^{-1}}$ for the edge-on case. In the same figure we compare the simulated FWHM with the one inferred from observations of high-z galaxies (Table 1). The bulk of the observed spectra have a [C II] line FWHM around 180 $\mathrm{km\,s^{-1}}$ that is compatible with that found from Althæa seen face-on. Note that Althæa has a dynamical mass $M_{\mathrm{dyn}} \simeq 10^{10}\,\mathrm{M}_{\odot}$, while the dynamical masses of the observed galaxies range from 10^{9}–$10^{11}\mathrm{M}_{\odot}$ (Capak et al. 2015).

We are interested in assessing the reliability of the dynamical mass estimates obtained from equation (16) as a function of [C II] line FWHM. The radius of the disc is computed from the [C II] image as $R \simeq r_{80}$, i.e. the effective radius of of the system containing 80 per cent of the total [C II] luminosity. For the three aforementioned stages of Althæa, $R \simeq 1$ kpc. It is convenient to define the 'mass-error-function', i.e.

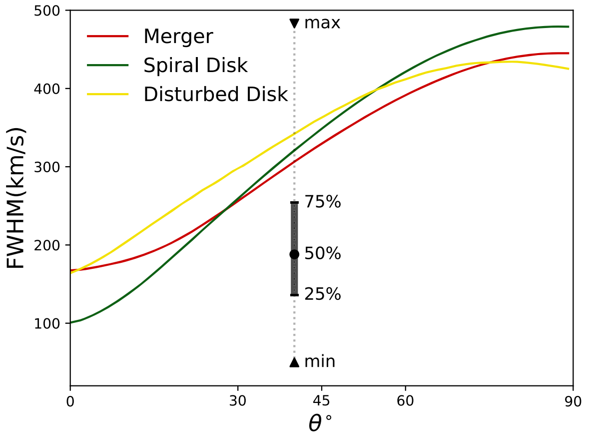

Figure 8. The FWHM of Althæa spectra as a function of inclination. Each line corresponds to a different evolutionary stage (see Fig. 6). As a reference, we overplot the statistical properties of the FWHM from observed in high-redshift galaxies (see Table 1).

$$\Delta M \equiv M^{\mathrm{est}}_{\mathrm{dyn}}/M_{\mathrm{dyn}}, \tag{17}$$

that parametrizes the error in the mass estimates using equation (16), that depends on γ. We calculate γ from our simulation depending on the stage of the evolution. The value of γ for the spiral disc, disturbed disc, and the merger stage is 1.78, 2.03, and 1.52, respectively.

In Fig. 9, we plot ΔM as a function of the FWHM for Althæa. In the left-hand panel estimates are performed by using the information

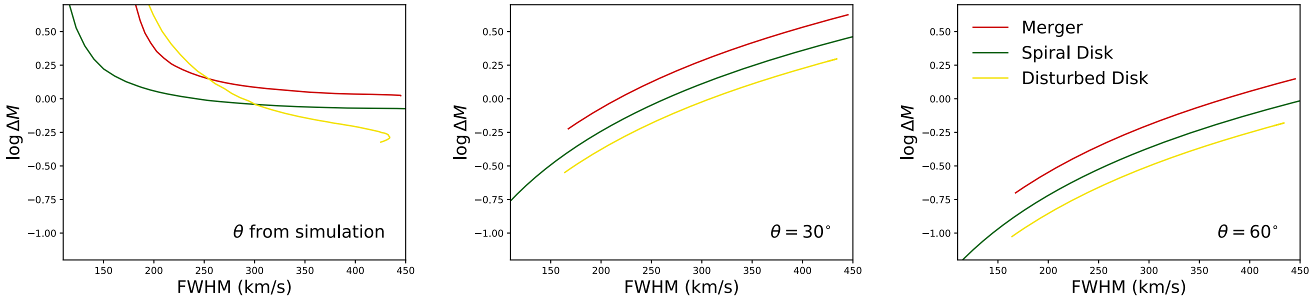

Figure 9. Analysis of the error in the dynamical mass determination using empirical estimates (16). The mass-error-function (ΔM, equation 17) is plotted as a function of the FWHM for known inclination, as calculated in the simulation (left-hand panel), and by assuming a fixed inclination of 30° (central panel) and 60° (right-hand panel). Different lines indicate the three selected evolutionary stages (see Fig. 6).

on the inclination obtained from the simulation. The minimum of $\Delta M = 0.4$ is found for large FWHM ($\geq 350\,\mathrm{km\,s^{-1}}$). At low FWHM, ΔM becomes very large as $M_{\mathrm{dyn}}^{\mathrm{est}} \propto 1/\sin^2\theta$. In all cases, we find $\Delta M > 1$ for low FWHM and $\Delta M < 1$ at high FWHM. This means that by using equation (16) we tend to underestimate (overestimate) the dynamical mass at high (low) FWHM, or, equivalently, inclinations (see the left-hand panel of Fig. 9).

It is interesting to calculate the mass-error-function for fixed inclinations, $\theta = 30^\circ$ and $\theta = 60^\circ$. These two values are generally assumed when θ cannot be directly determined from observations. This can happen when the spatial resolution does not allow us to constrain the inclination, as in Capak et al. (2015), that calculate the dynamical masses by assuming $\sin\theta = 0.45 - 1$. Results are shown in the central and right-hand panels of Fig. 9. For $\theta = 60^\circ$, $\Delta M < 1$ except for the high inclinations of the merger stage, while for $\theta = 30^\circ$ the dynamical mass is typically overestimated, up to a factor $\simeq 4$. The error of the estimate is comparable with the one reported for the sample of Capak et al. (2015), where the authors concluded that at $z > 5$ the dynamical masses are typically a factor of 3 greater than the stellar masses. This should be confronted with the analogous factor of 1.2–1.7 measured at $z \sim 1$–3 (Förster Schreiber et al. 2009).

The mass estimates equation (16) is based on the assumption that the galaxy has a smooth disc. However, our simulations show that high-z galaxies have more complex dynamical structures which result in correspondingly complex spectra. As observations are progressively becoming more precise, a better modelling of kinematics and velocity structure of the galaxies is required (e.g. Di Teodoro & Fraternali 2015).

5.2 Tully–Fisher relation for high-z galaxies

In Fig. 10, we plot the observed $L_{[\mathrm{CII}]}$–FWHM relation for the high-z galaxy sample in Table 1. The best fit to the data is

$$\log(L_{[\mathrm{CII}]}/\mathrm{L}_\odot) = \alpha \log(\mathrm{FWHM}/\mathrm{km\,s^{-1}}) + \beta, \tag{18a}$$

with

$$\alpha = 1.80 \pm 0.35, \tag{18b}$$

$$\beta = 4.32 \pm 0.78\,. \tag{18c}$$

The Pearson coefficient is $\simeq$0.74, suggesting a statistically reliable correlation between these two parameters. The three stages of Althæa (viewed face-on) are shown as triangles in this plot. They fall within 1σ from the best-fitting curve.

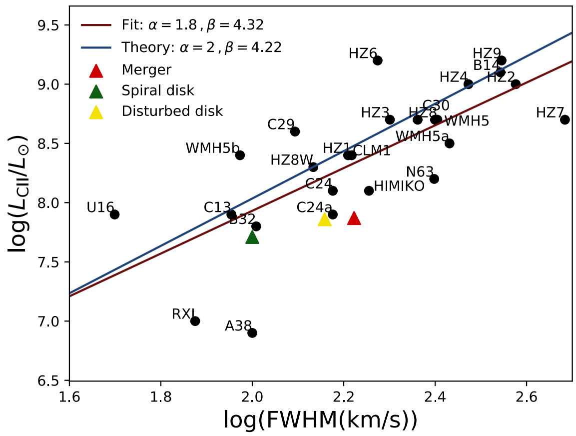

Figure 10. Correlation between $L_{\mathrm{C\,II}}$ and FWHM for the sample of observed high-z galaxies (black dots, Table 1). The red line indicates the fit to the data (functional form and parameters in equation 18). The blue line indicates the approximate relation given in equation (21) assuming $R = 1$ kpc and $\sin\theta = 0.5$.

Such relation resembles the Tully & Fisher (1977) relation. Its existence is not surprising because of the link between $L_{[\mathrm{CII}]}$ and the dynamical mass. As a rough estimate (see Pallottini et al. 2017a for an extensive discussion), we can assume a constant ratio between the total [C II] luminosity and the gas mass in a high-z galaxy; thus we can write

$$\kappa = \frac{L_{[\mathrm{C\,II}]}}{M_{\mathrm{g}}} = \frac{L_{[\mathrm{C\,II}]}}{f_{\mathrm{g}} M_{\mathrm{b}}}, \tag{19}$$

where f_{g} is the gas fraction of the baryonic mass (M_{b}). Using equation (16) and defining $f_{\mathrm{DM}} = M_{\mathrm{DM}}/M_{\mathrm{b}}$ as the ratio between dark matter and baryonic mass, the relation between $L_{[\mathrm{CII}]}$ and the FWHM of the line reads as

$$L_{[\mathrm{C\,II}]} = \frac{\kappa R}{G}\left(\frac{f_g}{1 + f_{\mathrm{DM}}}\right)\left(\frac{\mathrm{FWHM}}{\gamma \sin\theta}\right)^2. \tag{20}$$

Interestingly, this simple analytical expression is consistent with the empirical relation (equation 18). It is convenient to express equation (20) in terms of typical values found in high-z galaxies. Roughly, from our model we expect $\kappa = 0.1\mathrm{L}_\odot/\mathrm{M}_\odot$ (equation 1; see also Pallottini et al. 2017b), $\gamma \simeq 1.7$, $f_{\mathrm{g}} \simeq 0.5$, and $f_{\mathrm{DM}} \simeq 0.5$;

thus equation (20) can be written as

$$L_{[\mathrm{C\,II}]} \simeq 5.4 \times 10^7 \mathrm{L}_\odot \left(\frac{1}{\sin^2\theta}\right)\left(\frac{\mathrm{FWHM}}{100\,\mathrm{km\,s^{-1}}}\right)^2\left(\frac{R}{\mathrm{kpc}}\right). \qquad (21)$$

Further, fixing $R = 1$ kpc and $\sin\theta = 0.5$ we can express $\log L_{\mathrm{CII}}$ versus FWHM as in (18a) with parameters

$$\alpha = 2 \qquad (22a)$$

$$\beta = 4.22 \qquad (22b)$$

which is within 1σ from the fit (equation 18).

As a final remark, we note that in Fig. 10, there is a lack of data in both the low FWHM–high $L_{[\mathrm{CII}]}$ and the high FWHM–low $L_{[\mathrm{CII}]}$ regions. While the first occurence is physically motivated (it is unlikely that low-mass galaxies have large luminosities), the second one might arise from an observational bias. In fact, as [C II] is optically thin, its luminosity is constant with inclination. As a consequence, as the FWHM increases, the peak flux might drop below the detection threshold. We investigate this issue in the next section.

5.3 Observations of edge-on versus face-on galaxies

We now check the detectability of [C II] line for face-on and edge-one inclinations by performing mock ALMA observability simulations. We select the spiral disc evolutionary stage, i.e. when Althæa has luminosity $\log(L_{\mathrm{CII}}/\mathrm{L}_\odot) = 7.7$, similar to the one inferred for BD3299 (Maiolino et al. 2015; Carniani et al. 2017). As for BD3299 observation (Carniani et al. 2017), we assume a 10 h integration time with ALMA. We consider the edge-on and face-on inclinations and we re-bin the spectra with channel width in the range $100 \le \Delta v \le 300$, i.e. the typical one used when searching for lines in normal star-forming galaxies (SFR $\lesssim 100\mathrm{M}_\odot\,\mathrm{yr}^{-1}$).

The results of such analysis are shown in Fig. 11, where we also plot the 5σ noise level for some selected values of Δv. The face-on case is detected at $>5\sigma$ for all considered Δv, thus yielding a FWHM $\sim 100\,\mathrm{km\,s^{-1}}$, which is very similar to what is reported for BDF3299 in Carniani et al. (2017). However, the edge-on case with a larger intrinsic FWHM $= 479\,\mathrm{km\,s^{-1}}$ would be always undetected. Stated differently, the large l.o.s. velocities smear out the spectrum, making the detection more challenging if the galaxy is seen edge-on. This suggests that some of the non-detections reported at high z might be due to inclination effects when the target is close to edge-on. Note that here we are assuming that no beam smearing effects are in place, that is equivalent to assume that we marginally resolve the flux from the galaxy. This interpretation must be substantiated in a future work with better quantifying channel noise and spatial correlations of the ALMA beam.

6 SUMMARY AND CONCLUSIONS

We have studied the structural and kinematical properties of galaxies in the EoR ($z \ge 6$) as traced by the spectral profile of the [C II] emission line. The emission is computed from an analytical model accounting for gas cooling via the [C II] line (Dalgarno & McCray 1972; Wolfire et al. 1995; Vallini et al. 2013), and it includes CMB suppression of the line intensity (Da Cunha et al. 2013; Pallottini et al. 2015; Vallini et al. 2015).

First, we have applied our model to an idealized rotating disc galaxy, in order to investigate the effect of disc inclination (θ) and turbulent velocities (v_{t}) on the line profile. From this controlled environment, we have found that both large turbulent motions ($v_{\mathrm{t}}/\bar{v}_{\mathrm{c}} = \zeta > 0.5$, where $\bar{v}_{\mathrm{c}} \simeq 75\,\mathrm{km\,s^{-1}}$ is the galaxy circular velocity) and inclination angle $\theta < 75^\circ$ erase the double-peak line profile, expected from a rotating disc galaxy. In particular, we find that the peak flux of [C II] emission for face-on ($\theta = 0^\circ$) can be a factor 4 higher than in the edge-on view ($\theta = 90^\circ$). Next, we have used zoom-in cosmological simulations of a prototypical Lyman break galaxy (‘Althæa’; Pallottini et al. 2017b) to analyse the [C II] emission properties during its evolution in the redshift range $6 \lesssim z \lesssim 7$. Information on velocities, thermal, and turbulent motions included in the simulation, enabled us to build the [C II] surface brightness maps of Althæa and the synthetic spectra. At $z = 6.0$, Althæa has a total [C II] luminosity $L_{[\mathrm{C\,II}]} = 10^{8.19}\mathrm{L}_\odot$; this value accounts for a factor 2 suppression due to the CMB (see Fig. A1). At this epoch and viewed face-on, the [C II] emission map shows a smooth, disc-like structure with an extent of 2 kpc, on top of which are superimposed clumps with typical sizes of 100 pc. From the analysis of the [C II] line profile, we find that the effect of turbulent motions is to smooth out the spectrum by broadening the thermal profiles and to decrease the peak line intensity by 10 per cent. The degeneracy between turbulent motions and inclination is also present in the spectra of Althæa, that has a $\zeta \simeq 0.15$. The edge-on spectral profile of this stage is indicative of a rotating disc, i.e. it shows a double peak profile. Decreasing the inclination progressively washes out the disc signature from the profile and increases the peak flux by a factor of $\simeq 1.6$.

Studying the morphology of Althæa in the redshift range $6 \le z \le 7$, we have identified three main evolutionary stages with distinct spectral signatures: (I) merger, (II) spiral disc, and (III) disturbed disc. The irregular and choppy structure of the l.o.s. velocity profiles resulting from the simulations (see Fig. 7) translates into more structured [C II] line profiles with respect to the analytical model. Comparing the synthetic spectra for different stages of Althæa with the ones from the analytical model, we identify the spectral signatures of merger events, spiral arms, and extra-planar flows in the respective stage both in the face-on and edge-on profiles. The main signatures are summarized as follows:

Merging Satellites: the face-on profile of the merger stage of Althæa has a peak flux of 0.27 mJy, with a second peak in the blue part centred on $v = -100\,\mathrm{km\,s^{-1}}$. The major peak of the spectrum is due to the central disc, while the second peak is produced by the starless satellite. In the edge-on case, the spectrum shows an asymmetric double peak along with multiple peaks in the core due to co-rotating clumps. The signature of the merging satellite is visible as a broad peak (with spectral extent of $300\,\mathrm{km\,s^{-1}}$) in the red side of the double peak profile (centred around $v = +100\,\mathrm{km\,s^{-1}}$).

Spiral arms manifest in the asymmetric Gaussian profile of the face-on spectrum of the spiral disc stage. In the edge-on view, the signature of spiral arms is contained in the asymmetry of the double-peak profile corresponding to the rotating disc.

Extra-planar flows: the [C II] spectrum for the face-on view of disturbed disc stage features a quasi-symmetric Gaussian profile which has a broader core and more prominent wings compared to the spiral disc. Instead, in the edge-on view, extra-planar flows tend to erase the blue peak of the line profile, hence masking the rotating disc characteristic feature.

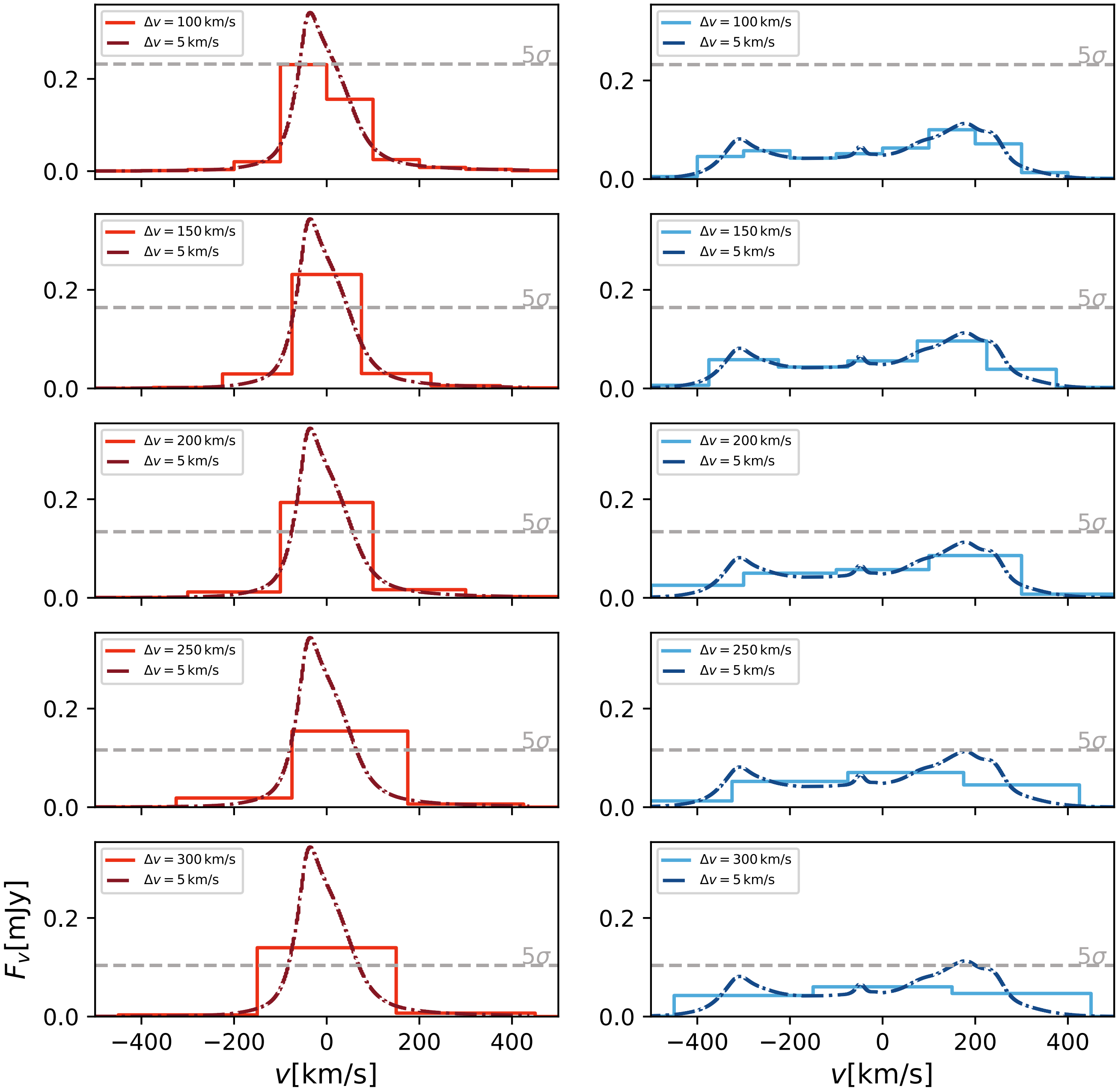

Figure 11. Comparison of the [C II] observability for face-on orientations (left-hand panels) versus edge-on (right-hand panels) ones when Althæa has $\log{(L_{\rm CII}/{\rm L}_{\odot})} = 7.7$, at $z = 6.28$ (spiral disc). From top to bottom the spectrum is re-binned with an increasing channel width (Δv). As a reference, the $\Delta v = 5\,{\rm km\,s}^{-1}$ case is reported in all panels. The dashed horizontal line corresponds to 5σ noise level, that is calculated by assuming a 10 hours ALMA observation.

Finally, we have discussed the observational implications of our analysis by comparing them to [C II] observations of high-z galaxies (see Table 1). The bulk of the observed spectra have FWHM $\sim 180\,{\rm km\,s}^{-1}$, that is compatible with face-on spectra of Althæa. Our key results are the following:

Dynamical mass estimates: we derived a generalized form of the dynamical mass versus [C II]–line FWHM relation (equation 16) which depends on the dynamical state of the galaxy. If precise information on the galaxy inclination is available, the returned mass estimate is accurate within a factor 2. If the inclination is not constrained, the error increases up to a factor of ≃4. These errors are due to the fact that high-z galaxies have a complex dynamical structure and the assumption of a smooth disc used in the derivation of equation (16) is not fully valid.

Tully–Fisher relation: We find a correlation between the $L_{\rm [CII]}$ and FWHM of the [C II] line by fitting the values for the sample of high-z galaxies, i.e. $L_{\rm [CII]} \propto ({\rm FWHM})^{1.80\,\pm\,0.35}$ (equation 18). This can be understood from simple physical arguments that are embedded in the relation given in equation (20). By fixing the inclination and radius of the galaxy, we find that such approximate theoretical expression (equation 21) is consistent with the empirical relation.

Inclination and detectability: We have performed mock ALMA simulations to check the detectability of [C II] line for face-on and edge-on views. We consider a fixed integration time (10 h) and rebin the spectra of the spiral disc stage with channel width in the range of $100\,\mathrm{km\,s^{-1}} \le \Delta v \le 300\,\mathrm{km\,s^{-1}}$. When seen face-on, the galaxy is always detected at $>5\sigma$; in the edge-on case it remains undetected because the larger intrinsic FWHM pushes the peak flux below the detection limit. This suggests that some of the non-detections reported for high-z galaxies might be due to inclination effects.

ACKNOWLEDGEMENTS

MK acknowledges the support from the ESO-SSDF 18/24 grant and hospitality by European Southern Observatory in Munich, where part of this work has been developed. MK, AF, and SC acknowledge support from the European Research Council (ERC) Advanced Grant INTERSTELLAR H2020/740120. LV acknowledges funding from the European Union's Horizon 2020 research and innovation program under the Marie Sklodowska-Curie grant agreement no. 746119. This research was supported by the Munich Institute for Astro- and Particle Physics (MIAPP) of the Deutsche Forschungsgemeinschaft (DFG) cluster of excellence 'Origin and Structure of the Universe'. We acknowledge use of the PYTHON programming language (Van Rossum & de Boer 1991), ASTROPY (Astropy Collaboration et al. 2013), CYTHON (Behnel et al. 2011), MATPLOTLIB (Hunter 2007), NUMPY (van der Walt, Colbert & Varoquaux 2011), PYMSES (Labadens et al. 2012), and SCIPY (Jones et al. 2001). Also, we are thankful to the anonymous referee for insightful comments and valuable suggestions.

REFERENCES

Agertz O., Kravtsov A. V., 2015, ApJ, 804, 18
Asplund M., Grevesse N., Sauval A. J., Scott P., 2009, ARA&A, 47, 481
Astropy Collaboration et al., 2013, A&A, 558, A33
Barkana R., Loeb A., 2001, Phys. Rep., 349, 125
Behnel S., Bradshaw R., Citro C., Dalcin L., Seljebotn D., Smith K., 2011, Comput. Sci. Eng., 13, 31
Behrens C., Pallottini A., Ferrara A., Gallerani S., Vallini L., 2018, MNRAS, 477, 552
Binney J., Tremaine S., 2008, Galactic Dynamics, 2nd ed. Princeton University Press, Princeton, NJ
Bouwens R. J. et al., 2015, ApJ, 803, 34
Bovino S., Grassi T., Capelo P. R., Schleicher D. R. G., Banerjee R., 2016, A&A, 590, A15
Bradač M. et al., 2017, ApJ, 836, L2
Capak P. L. et al., 2015, Nature, 522, 455
Carniani S. et al., 2017, A&A, 605, A42
Carniani S. et al., 2018a, MNRAS, 478, 1170
Carniani S., Maiolino R., Smit R., Amorín R., 2018b, ApJ, 854, L7
Da Cunha E. et al., 2013, ApJ, 766, 1, 13
Dalgarno A., McCray R. A., 1972, ARA&A, 10, 375
Dayal P., Ferrara A., 2018, Phys. Rep., 780, 1
De Looze I. et al., 2014, A&A, 568, A62
Di Teodoro E. M., Fraternali F., 2015, MNRAS, 451, 3021
Elitzur M., Asensio Ramos A., Ceccarelli C., 2012, MNRAS, 422, 1394
Fan X. et al., 2006, AJ, 132, 117
Förster Schreiber N. M. et al., 2009, ApJ, 706, 1364
Förster Schreiber N. M. et al., 2018, ApJS, 238, 21
Freeman K. C., 1970, ApJ, 160, 811
Gallerani S., Pallottini A., Feruglio C., Ferrara A., Maiolino R., Vallini L., Riechers D. A., Pavesi R., 2018, MNRAS, 473, 1909
Genzel R. et al., 2011, ApJ, 733, 101
Gnedin N. Y., 2000, ApJ, 535, 530
Goldsmith P. F., Langer W. D., Pineda J. L., Velusamy T., 2012, ApJS, 203, 13
Gong Y., Cooray A., Silva M., Santos M. G., Bock J., Bradford C. M., Zemcov M., 2012, ApJ, 745, 49
Grassi T., Bovino S., Schleicher D. R. G., Prieto J., Seifried D., Simoncini E., Gianturco F. A., 2014, MNRAS, 439, 2386
Habing H. J., 1968, Bull. Astron. Inst. Netherlands, 19, 421
Hashimoto T. et al., 2018, preprint (arXiv:1806.00486)
Hunter J. D., 2007, Comput. Sci. Eng., 9, 90
Jiang L. et al., 2016, ApJ, 816, 16
Jones E. et al., 2001, SciPy: Open source scientific tools for Python. Available at: http://www.scipy.org/
Jones G. C., Willott C. J., Carilli C. L., Ferrara A., Wang R., Wagg J., 2017, ApJ, 845, 175
Katz H. et al., 2019, prepint (arXiv:1901.01272)
Keenan F. P., Lennon D. J., Johnson C. T., Kingston A. E., 1986, MNRAS, 220, 571
Kennicutt R. C. Jr, 1998, ApJ, 498, 541
Knudsen K. K., Richard J., Kneib J.-P., Jauzac M., Clément B., Drouart G., Egami E., Lindroos L., 2016, MNRAS, 462, L6
Labadens M., Chapon D., Pomaréde D., Teyssier R., 2012, in Ballester P., Egret D., Lorente N. P. F., eds, ASP Conf. Ser. Vol. 461, Astronomical Data Analysis Software and Systems XXI. Astron. Soc. Pac., San Francisco, p. 837
Laporte N. et al., 2017, ApJ, 837, L21
Leung T. K. D. et al., 2019, ApJ, 871, 85
Luhman M. L. et al., 1998, ApJ, 504, L11
Luhman M. L., Satyapal S., Fischer J., Wolfire M. G., Sturm E., Dudley C. C., Lutz D., Genzel R., 2003, ApJ, 594, 758
Madau P., Haardt F., Rees M. J., 1999, ApJ, 514, 648
Maiolino R. et al., 2015, MNRAS, 452, 54
Malhotra S. et al., 1997, ApJ, 491, L27
Matthee J. et al., 2017, ApJ, 851, 145
McGreer I. D., Mesinger A., Fan X., 2011, MNRAS, 415, 3237
Olsen K., Greve T. R., Narayanan D., Thompson R., Davé R., Niebla Rios L., Stawinski S., 2017, ApJ, 846, 105
Ouchi M. et al., 2013, ApJ, 778, 102
Pallottini P. et al., 2019, MNRAS, 487, 1689
Pallottini A., Gallerani S., Ferrara A., Yue B., Vallini L., Maiolino R., Feruglio C., 2015, MNRAS, 453, 1898
Pallottini A., Ferrara A., Gallerani S., Vallini L., Maiolino R., Salvadori S., 2017a, MNRAS, 465, 2540
Pallottini A., Ferrara A., Bovino S., Vallini L., Gallerani S., Maiolino R., Salvadori S., 2017b, MNRAS, 471, 4128
Pentericci L. et al., 2016, ApJ, 829, L11
Schmidt M., 1959, ApJ, 129, 243
Simons R. C. et al., 2019, ApJ, 874, 59
Smit R. et al., 2014, ApJ, 784, 58
Smit R. et al., 2018, Nature, 553, 178
Stacey G. J., Geis N., Genzel R., Lugten J. B., Poglitsch A., Sternberg A., Townes C. H., 1991, ApJ, 373, 423
Suginohara M., Suginohara T., Spergel D. N., 1999, ApJ, 512, 547
Teyssier R., 2002, A&A, 385, 337
Tully R. B., Fisher J. R., 1977, A&A, 500, 105
Vallini L., Gallerani S., Ferrara A., Baek S., 2013, MNRAS, 433, 1567
Vallini L., Gallerani S., Ferrara A., Pallottini A., Yue B., 2015, ApJ, 813, 36
Vallini L., Pallottini A., Ferrara A., Gallerani S., Sobacchi E., Behrens C., 2018, MNRAS, 473, 271
van der Walt S., Colbert S. C., Varoquaux G., 2011, Comput. Sci. Eng., 13, 22
Van Rossum G., de Boer J., 1991, CWI Q., 4, 283
Wang R. et al., 2013, ApJ, 773, 44
Willott C. J., Carilli C. L., Wagg J., Wang R., 2015, ApJ, 807, 180
Wolfire M. G., Hollenbach D., McKee C. F., Tielens A. G. G. M., Bakes E. L. O., 1995, ApJ, 443, 152

APPENDIX: CMB EFFECT

Suppresion due to the CMB is crucial for a correct analysis of the FIR emission coming from high redshifts (Da Cunha et al. 2013; Pallottini et al. 2015; Vallini et al. 2015). In Fig. A1, we compare the [C II] surface brightness maps with (see equation 3) and without ($\eta = 1.0$) the inclusion of CMB suppression. Primarily, the CMB suppresses the extended part of the signal, that is typically produced by diffuse gas ($n \lesssim 5\,\mathrm{cm}^{-3}$). Note that some degree of suppression is present also for high-density gas ($n \sim 100\,\mathrm{cm}^{-3}$), i.e. those dense regions that have kinetic temperature close to T_{CMB}. This fact can be understood from the trend of η with gas density and temperature (see Fig. 1). As a consequence of CMB quenching, in this specific case the total luminosity is reduced by about a factor of $\simeq$2, i.e. from $10^{8.52}\mathrm{L}_{\odot}$ to $10^{8.19}\mathrm{L}_{\odot}$.

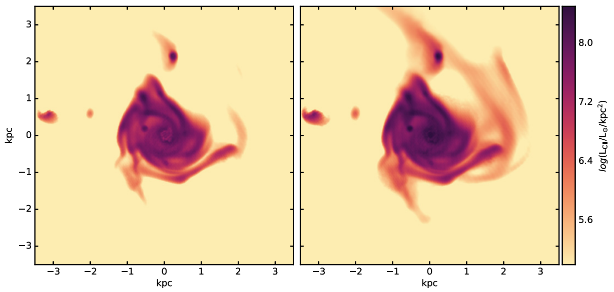

Figure A1. [C II] surface brightness of Althæa at redshift $z = 6$. In the left-hand panel ($L_{\mathrm{tot}} = 10^{8.19}\mathrm{L}_{\odot}$) the effect of CMB is included while in the right-hand panel ($L_{\mathrm{tot}} = 10^{8.52}\mathrm{L}_{\odot}$) it is not.

This paper has been typeset from a TEX/LATEX file prepared by the author.